

Showcasing research from Professor Y. Chris Li's laboratory, Department of Chemistry, University at Buffalo, USA.

Direct conversion of bicarbonate capture solution into multi-carbon products in a plasma electrochemical system

A plasma-catalytic process is reported to convert bicarbonate molecules into carbon monoxide and carbon dioxide. When paired with a subsequent electrochemical process, this platform enables the conversion of bicarbonate to ethylene with high Faradaic efficiency. This integrated plasma-electrochemical approach simplifies separate carbon capture and conversion steps, offering a more environmentally friendly process.

Image reproduced by permission of Yuguang C. Li from *Green Chem.*, 2026, **28**, 4466.

As featured in:



See Yuguang C. Li *et al.*, *Green Chem.*, 2026, **28**, 4466.



Cite this: *Green Chem.*, 2026, **28**, 4466

## Direct conversion of bicarbonate capture solution into multi-carbon products in a plasma electrochemical system

Xiaoli Ge,<sup>a</sup> Gina DelMonache,<sup>a</sup> Shwetha Prakash,<sup>a</sup> Mayuresh Janpandit,<sup>a</sup> Pratahdeep Gogoi,<sup>a</sup> Zhaoqiang Li<sup>b</sup> and Yuguang C. Li<sup>a</sup>\*

Atmospheric CO<sub>2</sub> capture has become an increasingly important industrial process in response to climate challenges. Conventional CO<sub>2</sub> capture processes often require an energy-intensive step to regenerate the capture solution, typically a (bi)carbonate solution. Developing new chemical processes that directly convert the capture solution can bypass this energy-demanding regeneration step and yield valuable multi-carbon products. This study introduces a hybrid nonthermal plasma–electrochemical system that enables the direct conversion of bicarbonate molecules into ethylene in high yield. The captured bicarbonate solution is activated directly by solvated electrons and radical species generated from the plasma. The effects of counter cations in the HCO<sub>3</sub><sup>−</sup> solution and carrier gas in the plasma reactor on the composition of plasma-activated intermediates, including O<sub>2</sub>, H<sub>2</sub>, CO, CO<sub>2</sub>, and CH<sub>4</sub>, were examined using NMR and GC/MS analyses. These mixed plasma-activated gaseous products, containing up to 73.5 vol% CO and CO<sub>2</sub>, were subsequently introduced into an electrolyzer, achieving a C<sub>2+</sub> faradaic efficiency of 83.7% at 200 mA cm<sup>−2</sup> with 59.5% ethylene selectivity. This approach demonstrates the direct transformation of carbon capture solutions into high-yield C<sub>2+</sub> products and establishes a platform for the chemical activation of otherwise inert molecules.

Received 9th October 2025,  
Accepted 16th December 2025

DOI: 10.1039/d5gc05361g

[rsc.li/greenchem](http://rsc.li/greenchem)

### Green foundation

1. This work illustrated a new approach for the direct valorization of bicarbonate capture solution into ethylene. This approach simplifies two separate carbon capture and conversion steps and operates under ambient conditions completely, thereby minimizing both environmental impacts and energy consumption.
2. A faradaic efficiency of 83.7% was achieved when converting to C<sub>2+</sub> products at −200 mA cm<sup>−2</sup> with 59.5% ethylene selectivity – one of the highest selectivity performances for the direct conversion of bicarbonate into ethylene.
3. Future work will explore further improving energy efficiency and production throughput of the system. Technoeconomic analysis can be conducted to identify the pinch point of the system.

## 1. Introduction

As the global CO<sub>2</sub> level continues to rise due to industrial and human activities, environmental problems and energy crises are an ever-pressing problem for our society.<sup>1–3</sup> Therefore, capturing and converting atmospheric CO<sub>2</sub> into high-value chemicals has become a critical research area.<sup>4</sup> The electrochemical reduction of carbon dioxide, powered by renewable electricity, provides a promising approach to realizing carbon neutrality while generating highly valuable products and fuels, such as

ethylene and ethanol.<sup>5</sup> However, industrial-scale CO<sub>2</sub> electrolyzers, despite their efficiency, require a CO<sub>2</sub> stream of high purity, which typically comes from CO<sub>2</sub> capture from air or an industrial flue gas stream. These processes demand significant energy input, especially for CO<sub>2</sub> regeneration such as that in drying and calcination processes.<sup>4,6</sup>

Considering energy consumption, researchers are exploring strategies to directly couple upstream CO<sub>2</sub> capture with a CO<sub>2</sub> conversion device, realizing *in situ* CO<sub>2</sub> regeneration and conversion from CO<sub>2</sub> capture products, such as bicarbonate or carbonate solution.<sup>7–9</sup> Compared with a gas-fed CO<sub>2</sub> electrolyzer, a liquid-fed (bi)carbonate electrolyzer can significantly reduce system complexity and approach high levels of CO<sub>2</sub> utilization. Li *et al.* developed a membrane electrode assembly (MEA) system based on a bipolar membrane (BPM) that can convert

<sup>a</sup>Department of Chemistry, University at Buffalo, State University of New York, Buffalo, New York, 14260, USA. E-mail: [yuguangli@buffalo.edu](mailto:yuguangli@buffalo.edu)

<sup>b</sup>Department of Physics, Faculty of Arts and Sciences, Beijing Normal University, Zhuhai, Guangdong, 519087, P.R. China



carbonate solution directly to produce pure syngas with a  $H_2 : CO$  ratio of *ca.* 3 : 1 and achieved 100% carbon utilization from the carbonate solution.<sup>10</sup> The operation of this device is based on the reaction between the proton generated from the BPM and the carbonate solution to produce  $CO_2$  *in situ* locally on the catalyst's surface. Several follow-up studies have since investigated the influence of BPM, interlayer, or catalyst designs on the local pH with the goal of increasing the amount of *in situ* generated  $CO_2$ .<sup>11–13</sup> The Hatzell group demonstrated a Ni-based single-atom electrocatalyst integrated with a BPM-based MEA to directly convert bicarbonate into CO, achieving a 93% CO FE.<sup>12</sup> However, these (bi)carbonate electrolyzers still face some limitations. First, their selectivity for  $C_{2+}$  products is typically lower compared to conventional  $CO_2RR$  electrolyzers due to the low  $CO_2$  concentration at the catalyst surface. Second, (bi)carbonate electrolyzers require a BPM or a cation exchange membrane (CEM) to generate or transport  $H^+$  for  $CO_2$  generation, which can increase the rate of the competing hydrogen evolution reaction. From a practical perspective, the dissociation of water within the BPM and the thickness of the BPM may lead to high overall cell voltages, which could pose challenges for scaling up. To continue advancing the field of direct bicarbonate conversion into value-added chemicals, new methods of activating bicarbonate solutions are needed.

In recent years, researchers have demonstrated the applications of non-thermal plasma technology in a number of different catalysis reactions under ambient conditions.<sup>14–16</sup> Non-thermal plasma or room-temperature plasma is typically generated *via* a dielectric barrier discharge mechanism, and it can activate thermodynamically stable molecules like  $CO_2$  or  $N_2$  into reactive species, allowing subsequent conversion into value-added compounds. For example, plasma conversion has been demonstrated by activating  $CH_4$  or  $H_2$  alongside  $CO_2$  to generate hydrocarbons.<sup>17–20</sup> While plasma chemistry provides sufficient energy to break up any chemical bonds, reaction selectivity control is often very difficult. Therefore, incorporating catalysts into plasma reactors has been an ongoing research area to stabilize and facilitate the binding of reactants to steer the reaction outcome.<sup>17,18,20</sup> The continued development of plasma catalysis, especially in the direction of controlling reaction selectivity, could bring significant breakthroughs for catalysis science. Given the success of plasma  $CO_2$  catalytic conversion, we posit that bicarbonate molecules, which are similar to  $CO_2$  molecules, could also be activated *via* plasma and enable a new approach for direct bicarbonate solution conversion into value-added chemicals.

This work presents, for the first time, a new approach for coupling the plasma reactor with an electrolyzer to realize the reduction of plasma-activated bicarbonate, overcoming the limitations of *in situ* generated  $CO_2$  concentration in the BPM-based bicarbonate electrolyzer. We employ a cascading plasma–electrochemical approach where the plasma reactor activates the bicarbonate solution, and the electrochemical reactor steers the reaction outcome with an optimally designed catalyst. This approach allows us to separately control the acti-

vation of bicarbonate and its reaction selectivity. In the plasma reactor, the bicarbonate solution was activated into  $H_2$ ,  $O_2$ ,  $CH_4$ , and  $CO_2$ , which were then used in the  $CO_2RR$ . The mechanism of  $HCO_3^-$  activation in the solution phase *vs.* gas phase concentration was investigated by studying the effects of concentration, cations paired with  $HCO_3^-$ , and the carrier gas in the plasma reactor on the composition of plasma-activated products. Under optimized plasma conditions, our continuous plasma–electrochemical system with a tandem CuAg electrocatalyst achieved a total  $C_{2+}$  FE of 83.7% at  $200 \text{ mA cm}^{-2}$ . To the best of our knowledge, this is one of the highest FE values for the direct conversion of bicarbonate solutions into  $C_{2+}$  products. These results highlight the potential of our plasma–electrochemical approach to separately control the reaction activation and selectivity of thermodynamically stable chemicals, enabling new pathways for other chemical transformations, such as methane oxidation or plastic upcycling.

## 2. Experimental

All chemicals were directly used as received without further purification. The anion exchange membrane (AEM) was purchased from the Fuel Cell Store. Potassium hydroxide (KOH), potassium bicarbonate ( $KHCO_3$ ), and silver nitrate ( $AgNO_3$ ) were obtained from Thermo Scientific. Ni foam was purchased from MTI Corporation.

### Catalyst preparation

The Cu catalyst was prepared by sputtering a  $\sim 250 \text{ nm}$  Cu layer on a polytetrafluoroethylene (PTFE) membrane using the Kurt J. Lesker Company PRO Line PVD 75. The CuAg bimetallic catalyst was synthesized by a galvanic exchange method. A piece of Cu-PTFE was immersed in 5 mL of a 5 mM  $AgNO_3$  solution for 5 minutes at room temperature and then rinsed with deionized (DI) water and air dried.

### Material characterization

Scanning electron microscopy (SEM) and energy-dispersive X-ray spectroscopy (EDS) images were obtained using the Carl Zeiss AURIGA CrossBeam. The surface compositions were analyzed using X-ray photoelectron spectroscopy (XPS) with a PHI 5000 VersaProbe. Mass spectra were acquired using an Agilent 6890 series gas chromatography system coupled with a 5973 mass selective detector.  $^1H$ -NMR spectra were recorded using a Bruker 500 MHz system. Gas products were analyzed using gas chromatography (PerkinElmer, Clarus 590 GC) equipped with Carboxen 1000 and Mol Sieve 5A columns.

To evaluate radical formation under different cation electrolytes, 10 mM 2,2,6,6-tetramethylpiperidine 1-oxyl (TEMPO) was added to the plasma reactor under typical operational conditions. The concentration of the radicals generated from the plasma was extracted from electron spin resonance spectroscopy data.



### Plasma reactor design

Our custom-made plasma reactor consists of a glass bottle as the main container, a saturated  $\text{KHCO}_3$  solution as the reactant, a copper rod as the high-voltage electrode, and nickel foam as the ground electrode. The voltage profile of the plasma was measured with an oscilloscope and a high-voltage probe.

### Electrochemical experiments

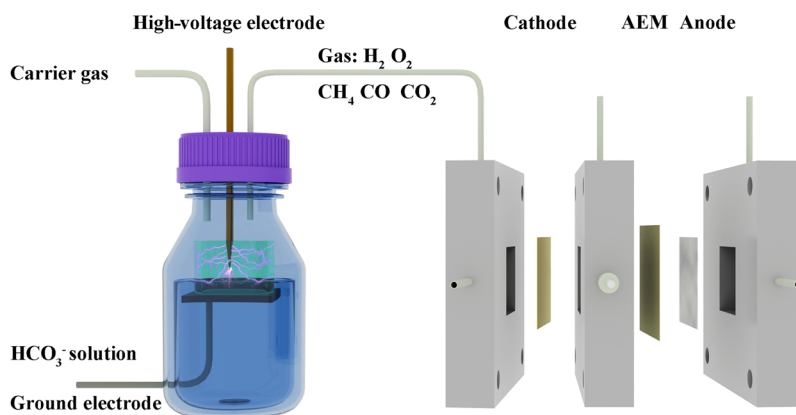
1.0 M KOH was used as both catholyte and anolyte and circulated with a peristaltic pump. The prepared Cu/CuAg-PTFE catalysts were applied as the cathode, Ni foam as the anode, and Ag/AgCl as the reference electrode. An anion exchange membrane (AEM) was placed between the anode and cathode. Electrochemical measurements were conducted using a SquidstatPlus Potentiostat (Admiral Instruments) in a flow cell. The  $\text{CO}_2$ RR was performed at current densities of  $-100$ ,  $-200$ ,  $-300$ , and  $-400$   $\text{mA cm}^{-2}$ . Different carrier gases from the plasma reactor were used as the inlet.

For the plasma production rate calculation (Fig. 2c–f and S6, S7), the  $\text{H}_2$  and  $\text{O}_2$  from the carrier gas were first subtracted. The inlet  $\text{CO}_2$ RR stream (the outlet of the plasma reactor) consists of a mixture of  $\text{CO}_2$ ,  $\text{CO}$ ,  $\text{O}_2$ ,  $\text{CH}_4$ , and  $\text{H}_2$ , some of which are also products of the  $\text{CO}_2$ RR. The FE values reported in Fig. 3, 4 and S12 are calculated by subtracting the contributions of  $\text{CO}$ ,  $\text{CH}_4$ , and  $\text{H}_2$  from the plasma reaction; more specifically, GC measurements were conducted before every electrochemical  $\text{CO}_2$ RR to determine the amount of  $\text{CO}$ ,  $\text{CH}_4$ , and  $\text{H}_2$  from the plasma reaction. The  $\text{CO}$ ,  $\text{CH}_4$ , and  $\text{H}_2$  contributions from plasma are subtracted from the  $\text{CO}_2$ RR results to calculate the FE. For the stability test, a constant current density of  $-200$   $\text{mA cm}^{-2}$  was applied. The  $j$ - $V$  curves were obtained through chronoamperometry experiments at different voltages for 5 minutes. The current densities averaged stable values in the final minute. All experiments were conducted in triplicate.

## 3. Results and discussion

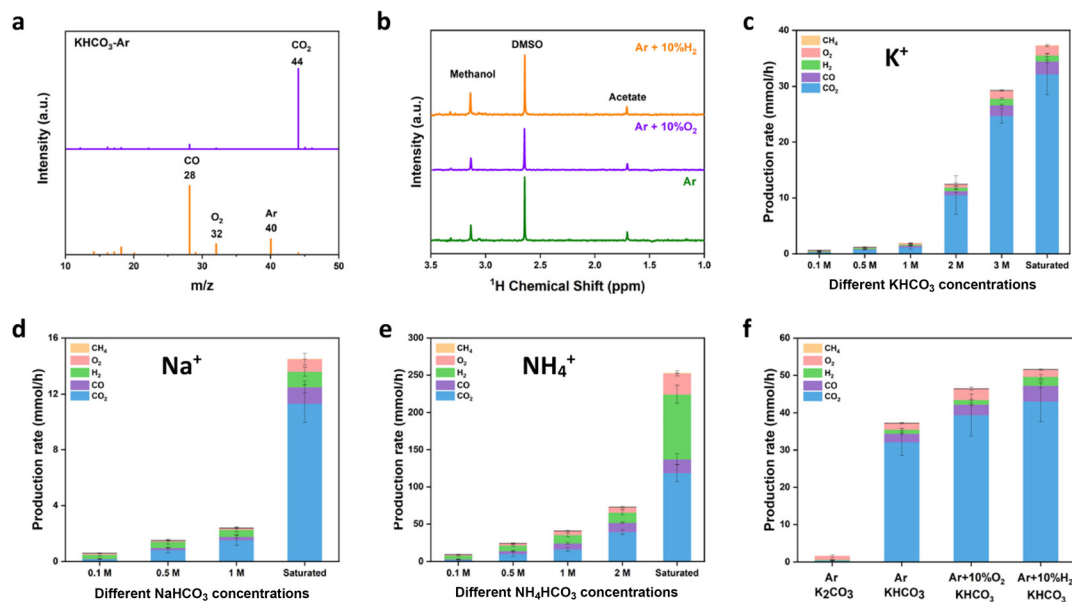
The plasma–electrochemical system setup is illustrated in Fig. 1. Our custom plasma reactor is based on a dielectric barrier discharge mechanism and it is modified from previous reports.<sup>21–23</sup> A copper nail is used as the high-voltage electrode, while nickel foam acts as the ground electrode, facilitating plasma discharge at the  $\text{HCO}_3^-$  solution interface. The plasma-activated gas products were then purged into the flow cell for the  $\text{CO}_2$ RR. To maintain a stable flow rate for the  $\text{CO}_2$ RR, a carrier gas at 5 sccm was used to purge the plasma reactor bottle into the electrochemical reactor. As illustrated in Fig. S1a–c, during a plasma strike, visible vapor is generated inside the bottle. These vapors lead to plasma discharge in random orientation due to the water droplet next to the copper electrode creating a path for discharge. To maintain a consistent plasma output, we added a glass tube container around the copper electrode to constrain the plasma strikes, making them more concentrated towards the solution surface (Fig. S1d–f). Gas chromatography–mass spectrometry (GC–MS) and  $^1\text{H}$  nuclear magnetic resonance (NMR) spectroscopy were applied to qualitatively identify the plasma-activated carbonaceous reactants in the gas and liquid phase, respectively. As shown in Fig. 2a and Fig. S2 and S3,  $\text{O}_2$ ,  $\text{CO}$ ,  $\text{CO}_2$ , and  $\text{CH}_4$  were detected with GC–MS.  $\text{H}_2$  was also detected with GC equipped with an FID detector (Fig. S2). These initial results confirm that plasma can efficiently activate the  $\text{HCO}_3^-$  molecule into smaller fragments. A plasma–electrochemical scheme will be a viable approach for the direct conversion of bicarbonate into value-added products. Given the plasma discharge at the  $\text{HCO}_3^-$  solution interface, the bicarbonate solution inside the plasma reactor was analyzed and methanol and acetate were identified (Fig. 2b). However, methanol and acetate remain in the bicarbonate solution bottle and do not participate in the subsequent electrochemical reaction.

Fig. S11 shows the time-dependent production rates of  $\text{H}_2$ ,  $\text{O}_2$ ,  $\text{CH}_4$ , and  $\text{CO}$  species, which exhibit excellent stability.



**Fig. 1** Illustration of a continuous-flow plasma–electrochemical setup for bicarbonate activation. Bicarbonate ions are first activated in solution form;  $\text{CO}_2$  is generated and then converted into ethylene in the subsequent electrochemical reactor.





**Fig. 2** (a) GC-MS spectra of plasma gas products under Ar with saturated  $\text{KHCO}_3$  solutions. (b)  $^1\text{H-NMR}$  of plasma gas products under different carrier gases with saturated  $\text{KHCO}_3$  solutions. (c) Gas production rates under Ar with different  $\text{KHCO}_3$  concentrations. (d) Gas production rates under Ar with different  $\text{NaHCO}_3$  concentrations. (e) Gas production rates under Ar with different  $\text{NH}_4\text{HCO}_3$  concentrations. (f) Gas production rates under different carrier gases with saturated  $\text{KHCO}_3$  and  $\text{K}_2\text{CO}_3$ .

These results confirm that the plasma reactor is highly stable for continuous operation.

Isotopically labelled H, C and O experiments were conducted to identify the source of H, C and O. To identify the H source, for the electrochemically generated  $\text{CH}_4$  and  $\text{C}_2\text{H}_4$ , we performed  $\text{D}_2\text{O}$ -labeling experiments by replacing the catholyte ( $\text{KOH} + \text{H}_2\text{O}$ ) with  $\text{KOH} + \text{D}_2\text{O}$  in the electrochemical reactor. As shown in Fig. S4, almost exclusive  $\text{CD}_4$  ( $m/z = 20$ ) and  $\text{C}_2\text{D}_4$  ( $m/z = 32$ ) are detected in GC/MS, suggesting that water is the hydrogen source in the electrolyte rather than the plasma-generated  $\text{H}_2$ . To determine the source of carbon in our products, we conducted  $^{13}\text{C}$ -labeling experiments using  $\text{NaH}^{13}\text{CO}_3$  as the electrolyte in the plasma reactor. As shown in Fig. S5a, only  $^{13}\text{CO}_2$  ( $m/z = 45$ ) is detected in the mass spectra, confirming that the C source is derived from  $\text{HCO}_3^-$  and ruling out any potential carbon contamination. To identify the O source in  $\text{CO}_2$ , we conducted  $^{18}\text{O}$ -labeling experiments using  $\text{H}_2^{18}\text{O}$  in the plasma reactor. As shown in Fig. S5b, the mass spectra reveal the presence of a mixture of  $\text{C}^{16}\text{O}_2$  ( $m/z = 44$ ),  $\text{C}^{18}\text{O}^{16}\text{O}$  ( $m/z = 46$ ), and  $\text{C}^{18}\text{O}_2$  ( $m/z = 48$ ), indicating that the O in  $\text{CO}_2$  originates from both  $\text{HCO}_3^-$  and  $\text{H}_2\text{O}$ . This is consistent with the expectation that both bicarbonate and water molecules are broken up during plasma discharge.

Since the plasma discharge can interact with bicarbonate molecules either in solution or gas vapor phase, we first set out to investigate the impacts of different solutions and carrier gas conditions on the activation of bicarbonate under the plasma field. In the solution phase, we examine the  $\text{HCO}_3^-$  solution with different cations,  $\text{K}^+$ ,  $\text{Na}^+$ , and  $\text{NH}_4^+$ , and quantify the respective plasma gas products. The yield of different species generated in the plasma reactor was quantified by GC

at various concentrations of  $\text{KHCO}_3$ ,  $\text{NaHCO}_3$ , and  $\text{NH}_4\text{HCO}_3$ , as shown in Fig. 2c–e. Under identical concentration conditions, the decomposition rate of  $\text{HCO}_3^-$  solution generally follows the trend of  $\text{NH}_4\text{HCO}_3 > \text{NaHCO}_3 > \text{KHCO}_3$ . If the salt concentrations are increased further, maximum production of  $\text{CO}_2$  is reached in the saturated form of each solution. Of particular interest to note is that the decomposition rate of  $\text{NH}_4\text{HCO}_3$  is orders of magnitude larger than that of  $\text{NaHCO}_3$  and  $\text{KHCO}_3$ . The reported thermal decomposition temperatures of  $\text{KHCO}_3$  and  $\text{NaHCO}_3$  are well over  $100\text{ }^\circ\text{C}$ ,<sup>24,25</sup> whereas the thermal decomposition temperature of  $\text{NH}_4\text{HCO}_3$  is reported at *ca.*  $30\text{ }^\circ\text{C}$ .<sup>26</sup> Thus, the gas produced from plasma-activated  $\text{NH}_4\text{HCO}_3$  has a large contribution from thermal decomposition. We conducted control experiments to determine the contribution of thermal decomposition in  $\text{KHCO}_3$  and  $\text{NaHCO}_3$ . Fig. S9 reveals that only  $\text{CO}_2$  was produced when heating a  $\text{NaHCO}_3$  solution to  $80\text{ }^\circ\text{C}$ , with the production rate reaching less than 20% of that achieved *via* plasma activation. This suggests that  $\text{CO}_2$  produced from  $\text{KHCO}_3$  and  $\text{NaHCO}_3$  are predominantly caused by plasma and to a small extent by thermal decomposition due to local temperature increases. The difference in the  $\text{HCO}_3^-$  solution decomposition rate when comparing  $\text{Na}^+$  vs.  $\text{K}^+$  may be attributed to the change in the solution dielectric constant due to cation disruption to the water network.<sup>27</sup>

To further evaluate the  $\text{HCO}_3^-$  activation mechanism, electron spin resonance (EPR) spectroscopy was conducted to probe the formation of plasma-generated radicals and to evaluate the relationship between different cations and radical generation. 2,2,6,6-Tetramethylpiperidine 1-oxyl (TEMPO) was used as a radical scavenger in the solution during the plasma reac-



tion; the amount of TEMPO consumed is a relative indicator of the radicals generated during the plasma reaction. As shown in Fig. S10, the TEMPO concentration in EPR follows a trend of  $\text{NH}_4^+ < \text{K}^+ < \text{Na}^+$ , indicating that the  $\text{NH}_4\text{HCO}_3$  solution promotes the highest level of radical generation under plasma conditions, followed by  $\text{K}^+$  and  $\text{Na}^+$ . This trend is consistent with the production rates of plasma-generated gaseous products, as shown in Fig. 2, and confirms the impact of cations in solution.

The solubilities of  $\text{KHCO}_3$ ,  $\text{NaHCO}_3$ , and  $\text{NH}_4\text{HCO}_3$  at room temperature are 3.3 M, 1.2 M, and 2.7 M, respectively. Thus, under saturated concentrations, the bicarbonate activation rate of  $\text{KHCO}_3$  surpasses that of  $\text{NaHCO}_3$ . As shown in Tables S1 and S2, the saturated  $\text{NH}_4\text{HCO}_3$  solution produced a higher amount of CO and  $\text{CO}_2$  ( $137.38 \text{ mmol h}^{-1}$ ) compared to saturated  $\text{NaHCO}_3$  and  $\text{KHCO}_3$ , but at the same time, it also produces a significant amount of hydrogen, reaching 33.1 vol% of the final gas outlet. The CO plus  $\text{CO}_2$  concentration in the plasma reactor outlet was highest with saturated  $\text{KHCO}_3$  at 92.4 vol% of the total gas produced without carrier gas, and 69.3 vol% with carrier gas. Details on the gas production rates are provided in Table S2. Consequently, a saturated  $\text{KHCO}_3$  solution was selected as the carbon source for plasma activation in all subsequent experiments.

To investigate the gas-phase bicarbonate activation, we explored the effect of different carrier gases (Fig. 2f). Ar was originally chosen as a carrier gas due to its inertness. In this study, we introduced 10%  $\text{H}_2$  and  $\text{O}_2$  gases into the plasma reactor with Ar as two general reducing and oxidizing reactants to tune the outcome of the plasma products. The gaseous species observed under Ar with 10%  $\text{O}_2$  and Ar with 10%  $\text{H}_2$  were similar to those detected under pure Ar. However, the production rates varied significantly. In particular, the production rate of  $\text{CO}_2$  (Table S3) under Ar with 10%  $\text{H}_2$  approached  $43.11 \text{ mmol h}^{-1}$ , which is 34% higher than pure Ar. The amount of CO and  $\text{H}_2$  was also higher than the Ar baseline. The CO plus  $\text{CO}_2$  concentration in the outlet of the plasma reactor with saturated  $\text{KHCO}_3$  under Ar with 10%  $\text{H}_2$  (Table S4) reached a maximum of 73.5 vol% with carrier gas. The addition of  $\text{H}_2$  in the plasma gas stream likely stabilizes the  $\text{OH}^-$  product from the dissociation of bicarbonate ( $\text{HCO}_3^- \rightarrow \text{CO}_2 + \text{OH}^-$ ), thus promoting the overall bicarbonate activation and  $\text{CO}_2$  production. The activation of carbonate solution under Ar was also tested under similar plasma conditions; however, the  $\text{CO}_2$  production rate is much lower than that of saturated  $\text{KHCO}_3$  solution, likely due to the higher stability of  $\text{K}_2\text{CO}_3$ .

As demonstrated by the results thus far, bicarbonate ions can be effectively activated into  $\text{CO}_2$  by plasma activation. Given these findings, we conducted a  $\text{CO}_2\text{RR}$  experiment using a Cu-PTFE catalyst in a flow cell setting with 1 M KOH electrolyte. Cu was chosen as it is the only catalyst effective toward  $\text{C}_{2+}$  products.<sup>28–31</sup> A baseline  $\text{CO}_2\text{RR}$  was first established using pure  $\text{CO}_2$  from a gas cylinder to confirm the Cu catalyst product distribution under control conditions. As illustrated in Fig. 3a, the Cu-PTFE catalyst exhibited high  $\text{CO}_2\text{RR}$  selectivity

while suppressing the competitive HER. At current densities of  $-100$ ,  $-200$ ,  $-300$ , and  $-400 \text{ mA cm}^{-2}$ , the FE values of the  $\text{C}_{2+}$  products were 73.5%, 79.5%, 73.6%, and 61.4%, respectively, consistent with prior reports.<sup>32,33</sup> Subsequently, the plasma-activated  $\text{CO}_2$  was connected directly to the flow cell without any treatment and its performance is shown in Fig. S12. However, under this condition,  $\text{CH}_4$  and  $\text{H}_2$  were detected as major products. We posit that the water content in the plasma products participated in the reduction reaction directly leading to hydrogen evolution. Additionally, excess water content reduced the  $\text{CO}_2$  concentration, leading to  $\text{CH}_4$  production, as suggested by previous reports on  $\text{CO}_2$  concentration effects.<sup>34,35</sup>

To mitigate the impacts of water, we reevaluated the  $\text{CO}_2\text{RR}$  using a Drierite drying column in the gas line between the plasma outlet and the electrochemical reaction cell, with the obtained results shown in Fig. 3b. A maximum FE towards  $\text{C}_{2+}$  of 72.6% was achieved at  $-200 \text{ mA cm}^{-2}$ , which is within the standard deviation error of the control using pure  $\text{CO}_2$  (Fig. 3a). The small difference in performance may be due to the trace amount of water left in the gas stream. With the 10%  $\text{H}_2$  in the Ar carrier gas from the plasma reactor, the  $\text{C}_{2+}$  FE increased further to 82.6% at  $-200 \text{ mA cm}^{-2}$  (Fig. 3d). The improvement is likely due to the presence of CO in the gas stream, which is a key intermediate during the  $\text{CO}_2\text{RR}$  towards  $\text{C}_{2+}$  products. The FE performance of our plasma-electrochemical system matched or exceeded that of the baseline  $\text{CO}_2\text{RR}$  FE obtained with pure  $\text{CO}_2$ . It is also one of the best performances for direct bicarbonate conversion into ethylene in a  $\text{CO}_2$  electrolyzer.

To eliminate concerns that plasma-generated methanol and acetate may evaporate and dissolve into the catholyte to influence the accuracy of the  $\text{CO}_2\text{RR}$  FE, we conducted a controlled experiment by running our plasma-electrochemical system for 30 minutes without applying any current/voltage to the electrochemical cell. The catholyte was then collected and analyzed by  $^1\text{H-NMR}$  spectroscopy. As shown in Fig. S13, when there is no electrochemical reaction, no detectable methanol or acetate signals were observed.

To probe the reaction kinetics, electrochemical impedance spectroscopy (EIS) was applied to investigate the kinetic differences between plasma-activated bicarbonate vs. pure  $\text{CO}_2$  gas-fed electrolyzers. As demonstrated in Fig. 4a, the  $R_s$  values across all conditions were similar within experimental errors. However, all plasma-activated conditions exhibited significantly lower charge transfer resistance ( $R_{ct}$ ) values compared to pure  $\text{CO}_2$  gas-fed condition, indicating that the presence of mixed gases has enhanced the reaction kinetics. The fitted parameters and the equivalent circuit model for the EIS curves are provided in Table S6. The  $j$ - $V$  curves for all conditions are shown in Fig. 4b. All voltages reported here are half-cell voltages versus the Ag/AgCl reference electrode without  $iR$  correction. Compared to the  $\text{CO}_2$ -fed conditions, plasma-activated systems exhibited a positive shift in onset potential from  $-1.1 \text{ V}$  to  $-0.7 \text{ V}$  (see inset in Fig. 4b), indicating favorable reaction kinetics similar to the EIS results. This has likely been contrib-



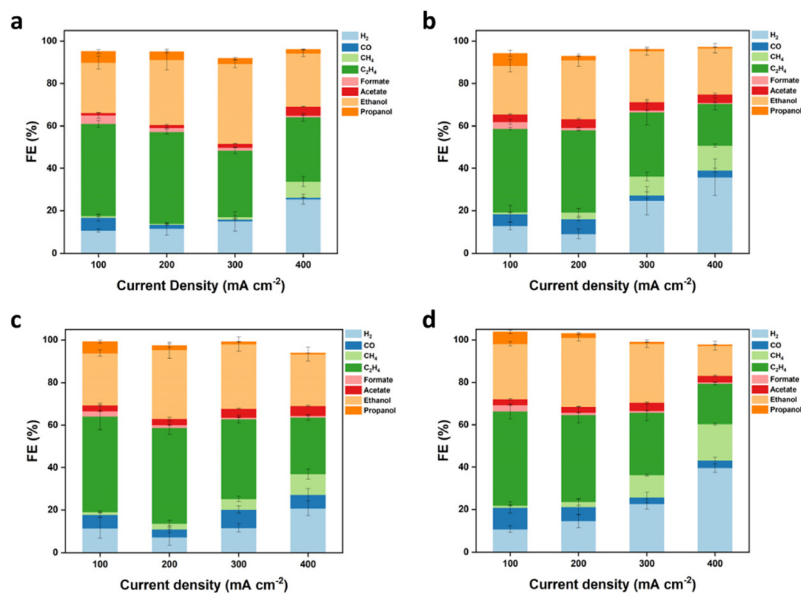


Fig. 3 The CO<sub>2</sub>RR FE of a sputtered Cu catalyst under different conditions. (a) Pure CO<sub>2</sub>. (b) Plasma-generated gases with Ar. (c) Plasma-generated gases with Ar + 10% H<sub>2</sub>. (d) Plasma-generated gases with Ar + 10% O<sub>2</sub>.

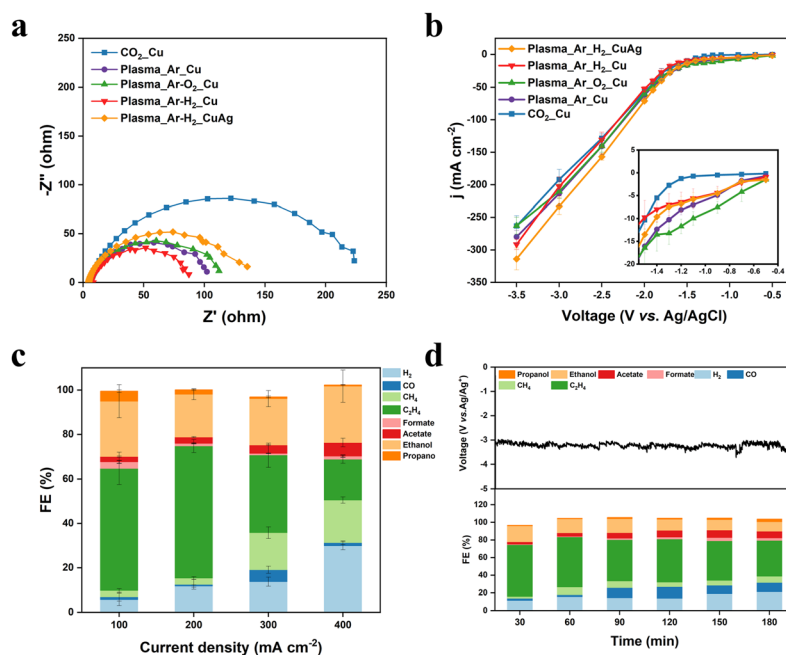


Fig. 4 (a) EIS spectra for the different CO<sub>2</sub>RR conditions. (b) The  $j$ - $V$  curves for different CO<sub>2</sub>RR conditions in the voltage range of  $-0.5$  to  $-3.5$  V vs. Ag/AgCl, with the inset showing the enlarged  $j$ - $V$  curves in the voltage range of  $-0.5$  to  $-1.5$  V vs. Ag/AgCl. (c) The FE for plasma-generated CO<sub>2</sub> with 90% Ar + 10% H<sub>2</sub> carrier gases and CuAg alloy prepared by the galvanic replacement reaction. (d) The stability test for the plasma-electrochemical configuration.

uted by the addition of CO in the gas stream, as CO<sub>2</sub> conversion into CO is often considered the rate-limiting step.<sup>36</sup>

As illustrated in the electrochemical results, the abundance of CO\* and CO-related intermediates can effectively enhance the CO<sub>2</sub>RR toward C<sub>2+</sub> products. Alloying Cu with CO-selective metals (*e.g.*, Au, Ag, Zn) has been demonstrated to facilitate a

sequential CO<sub>2</sub>-to-CO conversion for more efficient C-C coupling.<sup>37–40</sup> To further enhance the FE for C<sub>2+</sub> products, a CuAg bimetallic alloy was prepared *via* the galvanic substitution method. Representative scanning electron microscopy (SEM) and energy-dispersive X-ray spectroscopy (EDS) images (Fig. S14 and 15) confirmed the homogeneous distribution of Cu and Ag



in Cu-PTFE and CuAg-PTFE catalysts. X-ray photoelectron spectroscopy (XPS) provided further insight into the composition and electronic structure of synthesized Cu-PTFE and CuAg-PTFE. The Cu 2p spectra of Cu-PTFE (Fig. S16) exhibited two major peaks at 933.2 eV and 952.0 eV with a 2:1 area ratio, representing Cu 2p<sub>3/2</sub> and Cu 2p<sub>1/2</sub>. The peaks at 934.4 eV and 955.2 eV were ascribed to Cu<sup>2+</sup> species. These oxidized species were formed due to air exposure, which will be reduced to the metallic states under our electrochemical process. After alloying with Ag, the Cu 2p spectra (Fig. S17a) exhibited a positive shift, indicating altered surface electronic states. The Ag 3d XPS spectra (Fig. S17b) of CuAg-PTFE revealed peaks at 367.8 eV and 373.8 eV, corresponding to Ag 3d<sub>5/2</sub> and Ag 3d<sub>3/2</sub>, respectively. Fig. 4c demonstrates the CO<sub>2</sub>RR FE for the CuAg-PTFE, achieving a C<sub>2+</sub> FE of 83.7% at a current density of -200 mA cm<sup>-2</sup> with C<sub>2</sub>H<sub>4</sub> as the dominant product, reaching a selectivity of 59.5%. To evaluate the overall plasma-electrochemical system stability, a constant current experiment at -200 mA cm<sup>-2</sup> was conducted with gas products from the plasma reactor. Gas and liquid products from the CO<sub>2</sub>RR were collected every 30 minutes for product analysis. As illustrated in Fig. 4d, the system maintained a C<sub>2+</sub> FE of 62.3% after 180 minutes, demonstrating good operational stability. For comparison, we compiled recent reports on direct bicarbonate to C<sub>2+</sub> conversion in Table S7. Notably, our plasma-activated bicarbonate method achieves the highest FE for C<sub>2+</sub> products.<sup>41–48</sup> At the same time, we do acknowledge that our current energy efficiency is not sufficiently impactful and it is an area of improvement that we are actively working on.

## 4. Conclusions

The current work demonstrates a hybrid plasma-electrochemical system to enable the *ex situ* activation of bicarbonate solutions and optimization of the gas-phase composition for electrochemical CO<sub>2</sub> reduction. This approach provides an alternative route for direct bicarbonate conversion into value-added products compared to a BPM-based electrolyzer. The CO<sub>2</sub>-to-C<sub>2+</sub> selectivity is enhanced due to the addition of CO to the CO<sub>2</sub> stream, promoting C-C coupling. Under optimized plasma conditions with saturated KHCO<sub>3</sub> and Ar + 10% H<sub>2</sub>, a maximum CO/CO<sub>2</sub> concentration of 73.5% was achieved in the plasma reactor output. When coupled with a CO-selective CuAg-PTFE catalyst, the continuous plasma-electrochemical system realized a record C<sub>2+</sub> FE of 83.7% at -200 mA cm<sup>-2</sup> with C<sub>2</sub>H<sub>4</sub> selectivity reaching 59.5%. This plasma-electrochemical system can provide utilities beyond CO<sub>2</sub> reduction to facilitate the electrochemical synthesis of otherwise difficult-to-activate species, such as CH<sub>4</sub>, N<sub>2</sub>, or polymeric compounds, providing a new pathway to realize a carbon-neutral economy.

## Author contributions

Y. C. L. and X. G. conceptualized the idea of this project. The manuscript was written through contributions of all authors.

All authors have given approval to the final version of the manuscript.

## Conflicts of interest

There are no conflicts to declare.

## Data availability

The data that support this study are available within the article and its supplementary information (SI). Supplementary information: material synthesis and characterization studies, plasma reactor design, electrochemical experiments, Fig. S1–S17, and Tables S1–S7. See DOI: <https://doi.org/10.1039/d5gc05361g>.

## Acknowledgements

Y. C. L. would like to thank the Research Corporation for Science Advancement for funding support through the Cottrell Scholar Award.

## References

- W. Lai, Z. Ma, J. Zhang, Y. Yuan, Y. Qiao and H. Huang, *Adv. Funct. Mater.*, 2022, **32**, 2111193.
- W. Lai, Y. Qiao, J. Zhang, Z. Lin and H. Huang, *Energy Environ. Sci.*, 2022, **15**, 3603–3629.
- S. Jin, Z. Hao, K. Zhang, Z. Yan and J. Chen, *Angew. Chem.*, 2021, **133**, 20795–20816.
- D. W. Keith, G. Holmes, D. S. Angelo and K. Heidel, *Joule*, 2018, **2**, 1573–1594.
- J. E. Huang, F. Li, A. Ozden, A. Sedighian Rasouli, F. P. García de Arquer, S. Liu, S. Zhang, M. Luo, X. Wang and Y. Lum, *Science*, 2021, **372**, 1074–1078.
- S. Liu, J. Zhang, F. Li, J. P. Edwards, Y. C. Xiao, D. Kim, P. Papangelakis, J. Kim, D. Elder and P. De Luna, *Energy Environ. Sci.*, 2024, **17**, 1266–1278.
- D. J. Pimlott, Y. Kim and C. P. Berlinguette, *Acc. Chem. Res.*, 2024, **57**, 1007–1018.
- Q. Xia, K. Zhang, T. Zheng, L. An, C. Xia and X. Zhang, *ACS Energy Lett.*, 2023, **8**, 2840–2857.
- A. Ozden, F. P. García de Arquer, J. E. Huang, J. Wicks, J. Sisler, R. K. Miao, C. P. O'Brien, G. Lee, X. Wang and A. H. Ip, *Nat. Sustainability*, 2022, **5**, 563–573.
- Y. C. Li, G. Lee, T. Yuan, Y. Wang, D.-H. Nam, Z. Wang, F. P. García de Arquer, Y. Lum, C.-T. Dinh and O. Voznyy, *ACS Energy Lett.*, 2019, **4**, 1427–1431.
- G. Lee, A. S. Rasouli, B.-H. Lee, J. Zhang, Y. C. Xiao, J. P. Edwards, M. G. Lee, E. D. Jung, F. Arabyarmohammadi and H. Liu, *Joule*, 2023, **7**, 1277–1288.
- H. Song, C. A. Fernández, H. Choi, P.-W. Huang, J. Oh and M. C. Hatzell, *Energy Environ. Sci.*, 2024, **17**, 3570–3579.



- 13 Z. Zhang, D. Xi, Z. Ren and J. Li, *Cell Rep. Phys. Sci.*, 2023, **4**, 101662.
- 14 A. George, B. Shen, M. Craven, Y. Wang, D. Kang, C. Wu and X. Tu, *Renewable Sustainable Energy Rev.*, 2021, **135**, 109702.
- 15 J. Knezevic, T. Zhang, R. Zhou, J. Hong, R. Zhou, C. Barnett, Q. Song, Y. Gao, W. Xu and D. Liu, *J. Am. Chem. Soc.*, 2024, **146**, 12601–12608.
- 16 X. Ge, C. Zhang, M. Janpandit, S. Prakash, P. Gogoi, D. Zhang, T. R. Cook, G. I. Waterhouse, L. Yin and Z. Wang, *J. Am. Chem. Soc.*, 2024, **146**, 35305–35312.
- 17 L. Dou, Y. Liu, Y. Gao, J. Li, X. Hu, S. Zhang, K. K. Ostrikov and T. Shao, *Appl. Catal., B*, 2022, **318**, 121830.
- 18 N. Joshi and S. Loganathan, *ACS Omega*, 2023, **8**, 13410–13420.
- 19 C. De Bie, J. van Dijk and A. Bogaerts, *J. Phys. Chem. C*, 2016, **120**, 25210–25224.
- 20 S. Meng, L. Wu, M. Liu, Z. Cui, Q. Chen, S. Li, J. Yan, L. Wang, X. Wang and J. Qian, *AIChE J.*, 2023, **69**, e18154.
- 21 H. Zeghioud, P. Nguyen-Tri, L. Khezami, A. Amrane and A. A. Assadi, *J. Water Process Eng.*, 2020, **38**, 101664.
- 22 C. A. Aggelopoulos, *Chem. Eng. J.*, 2022, **428**, 131657.
- 23 G. T. Bae, J. Y. Kim, D. Y. Kim, E. Y. Jung, H. J. Jang, C.-S. Park, H. Jang, D. H. Lee, H.-K. Lee and H.-S. Tae, *Materials*, 2021, **14**, 7559.
- 24 M. Hartman, K. Svoboda, B. r. Čech, M. Pohořelý and M. Šyc, *Ind. Eng. Chem. Res.*, 2019, **58**, 2868–2881.
- 25 R. S. Gärtner, M. M. Seckler and G.-J. Witkamp, *Ind. Eng. Chem. Res.*, 2005, **44**, 4272–4283.
- 26 P. Nowak and J. Skrzypek, *Chem. Eng. Sci.*, 1989, **44**, 2375.
- 27 G. Das, S. Hlushak, M. C. Dos Ramos and C. McCabe, *AIChE J.*, 2015, **61**, 3053–3072.
- 28 D. Raciti and C. Wang, *ACS Energy Lett.*, 2018, **3**, 1545–1556.
- 29 G. L. De Gregorio, T. Burdyny, A. Loiudice, P. Iyengar, W. A. Smith and R. Buonsanti, *ACS Catal.*, 2020, **10**, 4854–4862.
- 30 F. Li, Y. C. Li, Z. Wang, J. Li, D.-H. Nam, Y. Lum, M. Luo, X. Wang, A. Ozden and S.-F. Hung, *Nat. Catal.*, 2020, **3**, 75–82.
- 31 Y. C. Li, Z. Wang, T. Yuan, D.-H. Nam, M. Luo, J. Wicks, B. Chen, J. Li, F. Li and F. P. G. De Arquer, *J. Am. Chem. Soc.*, 2019, **141**, 8584–8591.
- 32 Z. Wang, Y. Li, X. Zhao, S. Chen, Q. Nian, X. Luo, J. Fan, D. Ruan, B.-Q. Xiong and X. Ren, *J. Am. Chem. Soc.*, 2023, **145**, 6339–6348.
- 33 M. Luo, Z. Wang, Y. C. Li, J. Li, F. Li, Y. Lum, D.-H. Nam, B. Chen, J. Wicks and A. Xu, *Nat. Commun.*, 2019, **10**, 5814.
- 34 C. Deacon-Price, N. Chen, A. Lal, P. Broersen, E. J. Meijer and A. C. Garcia, *ChemCatChem*, 2025, e202401332.
- 35 X. Wang, A. Xu, F. Li, S.-F. Hung, D.-H. Nam, C. M. Gabardo, Z. Wang, Y. Xu, A. Ozden and A. S. Rasouli, *J. Am. Chem. Soc.*, 2020, **142**, 3525–3531.
- 36 W. Ma, X. He, W. Wang, S. Xie, Q. Zhang and Y. Wang, *Chem. Soc. Rev.*, 2021, **50**, 12897–12914.
- 37 C. Chen, Y. Li, S. Yu, S. Louisia, J. Jin, M. Li, M. B. Ross and P. Yang, *Joule*, 2020, **4**, 1688–1699.
- 38 F. A. Rollier, V. Muravev, N. Kosinov, T. Wissink, D. Anastasiadou, B. Ligt, L. Barthe, M. C. Figueiredo and E. J. Hensen, *J. Mater. Chem. A*, 2025, **13**, 2285–2300.
- 39 P. Guo, K. Liu, X. Liu, R. Liu and Z. Yin, *Energy Fuels*, 2024, **38**, 5659–5675.
- 40 A. Vasileff, C. Xu, Y. Jiao, Y. Zheng and S.-Z. Qiao, *Chem*, 2018, **4**, 1809–1831.
- 41 G. Lee, A. S. Rasouli, B.-H. Lee, J. Zhang, D. H. Won, Y. C. Xiao, J. P. Edwards, M. G. Lee, E. D. Jung and F. Arabyarmohammadi, *Joule*, 2023, **7**, 1277–1288.
- 42 S. Ma, Y. Kim, Z. Zhang, S. Ren, C. Donde, L. Melo, A. S. Williams, M. Stolar, E. R. Grant and C. P. Berlinguette, *ACS Energy Lett.*, 2024, **9**, 2326–2332.
- 43 Y. C. Li, G. Lee, T. Yuan, Y. Wang, D.-H. Nam, Z. Wang, F. P. García de Arquer, Y. Lum, C.-T. Dinh and O. Voznyy, *ACS Energy Lett.*, 2019, **4**, 1427–1431.
- 44 H. Song, C. A. Fernández, A. Venkataraman, V. D. Brandão, S. S. Dhingra, S. S. Arora, S. S. Bhargava, C. M. Villa, C. Sievers and S. Nair, *ACS Appl. Energy Mater.*, 2024, **7**, 1224–1233.
- 45 J. Lee, H. Liu and W. Li, *ChemSusChem*, 2022, **15**, e202201329.
- 46 B. N. Khirak, G. T. da Silva, J. Crane, C. P. O'Brien, M. R. Pepe, C. M. Gabardo, V. Golovanova, F. P. García de Arquer and C. T. Dinh, *Angew. Chem.*, 2025, **137**, e202509975.
- 47 J. Wang, Z. Zhang, W. Wu, Y. Liu, B. Dong, Y. Wang and Y. Wang, *ACS Energy Lett.*, 2023, **9**, 110–117.
- 48 S. Ma, H. Hu, F. Shen, Z. Chen and J. Hu, *Small*, 2025, e11008.

